The Astrophysical Journal Letters, 911:L7 (6pp), 2021 April 10 https://doi.org/10.3847/2041-8213/abf04e

Subproton-scale Intermittency in Near-Sun Solar Wind Turbulence Observed by the Parker Solar Probe

Rohit Chhiber[1,2], William H. Matthaeus[1], Trevor A. Bowen[3], and Stuart D. Bale[3,4]
[1] Department of Physics and Astronomy & Bartol Research Institute, University of Delaware, Newark, DE, USA; rohitc@udel.edu
[2] Heliophysics Science Division, NASA Goddard Space Flight Center, Greenbelt, MD, USA
[3] Space Sciences Laboratory, University of California Berkeley, Berkeley, CA, USA
[4] Physics Department, University of California Berkeley, Berkeley, CA, USA
Received 2021 February 9; revised 2021 March 10; accepted 2021 March 19; published 2021 April 13

Abstract

High time-resolution solar wind magnetic field data are employed to study statistics describing intermittency near the first perihelion ($\sim$35.6 $R_\odot$) of the Parker Solar Probe mission. A merged data set employing two instruments on the FIELDS suite enables broadband estimation of higher-order moments of magnetic field increments, with five orders established with reliable accuracy. The duration, cadence, and low noise level of the data permit evaluation of scale dependence of the observed intermittency from the inertial range to deep subproton scales. The results support multifractal scaling in the inertial range, and monofractal but non-Gaussian scaling in the subproton range, thus clarifying suggestions based on data near Earth that had remained ambiguous due to possible interference of the terrestrial foreshock. The physics of the transition to monofractality remains unclear but we suggest that it is due to a scale-invariant population of current sheets between ion and electron inertial scales; the previous suggestion of incoherent kinetic-scale wave activity is disfavored as it presumably leads re-Gaussianization that is not observed.

Unified Astronomy Thesaurus concepts: Solar wind (1534); Interplanetary turbulence (830); Magnetohydrodynamics (1964); Space plasmas (1544)

1. Introduction

Intermittency is an important feature in the theory of fluid and plasma turbulence (Sreenivasan & Antonia 1997; Matthaeus et al. 2015), and has gained increasing attention in the study of space plasmas, including the corona, the magnetosphere, and the solar wind (Abramenko et al. 2008; Chhiber et al. 2018; Bruno 2019). In each of these venues the emergence of localized sporadic features of the primitive fields is a consequence of the turbulent cascade of energy. The resulting coherent structures, of electric current density, vorticity, or density, are likely sites of enhanced kinetic dissipation, and heating (e.g., Osman et al. 2012). Therefore intermittency is crucial in terminating the cascade and heating the plasma. These coherent structures also compartmentalize the plasma, forming boundaries associated with distinctive flux tube "texture" that organizes quantities such as temperature, density, magnetic intensity, and energetic particles (Borovsky 2008; Tessein et al. 2013). Coherent structure forms in similar ways in hydrodynamics (Sreenivasan & Antonia 1997), magnetohydrodynamics (Wan et al. 2009), and plasmas (Burlaga 1991; Sorriso-Valvo et al. 1999; Matthaeus et al. 2015), with important differences, particularly approaching kinetic scales. Statistics in the plasma kinetic range provide insight regarding physical mechanisms responsible for dissipation (e.g., Goldstein et al. 2015; Chen 2016; Matthaeus et al. 2020), thus addressing fundamental questions related to coronal heating and acceleration of the solar wind (Fox et al. 2016).

Qualitatively speaking, monofractality is associated with structure that is non-space-filling but lacking a preferred scale over some range (i.e., scale invariance). In contrast, multifractality also implies non-space-filling structure but with at least one preferred scale within the relevant range (Frisch 1995). Such a distinction has likely implications for the preference of a system for specific classes of dissipative mechanisms. In the solar wind, and in collisionless plasmas in general, it remains unclear whether statistics at subproton scales remain strongly intermittent and multifractal, or become monofractal (Kiyani et al. 2009; Leonardis et al. 2013, 2016; Wan et al. 2016), or even return to Gaussianity (Koga et al. 2007; Wan et al. 2012; Wu et al. 2013; Chhiber et al. 2018; Roberts et al. 2020). These questions persist in part because of the scarcity of high time-resolution data at locations well separated from the terrestrial bow shock. Here we address these issues by employing high-resolution measurements of the magnetic field made by the Parker Solar Probe (PSP) in near-Sun solar wind (Fox et al. 2016).

2. Theoretical Background

In turbulence, considerable information is contained in the statistics of fluctuations and increments of the primitive variables. These are velocity in hydrodynamics, velocity and magnetic fluctuations in magnetohydrodynamics (MHD), density for compressible flows, and additional variables for complex fluids and plasmas. The basic second-order statistics include two-point correlations, their Fourier transforms, i.e., wavenumber (k) spectra (Matthaeus & Goldstein 1982), and the second-order structure functions (Burlaga 1991). These and other relevant statistics are moments of the underlying joint probability distributions functions (PDFs; e.g., Monin & Yaglom 1971). Second-order moments describe the distribution of energy over spatial scales $\ell \sim 1/k$. To describe the spatial concentration of energy in *intermittent* structures, we go beyond second-order statistics and consider *higher-order* moments of PDFs (e.g., Frisch 1995).

The original K41 similarity hypothesis (Kolmogorov 1941) postulates the statistical behavior of longitudinal velocity increments at spatial lag ℓ, namely, $\delta u_\ell = \hat{\boldsymbol{\ell}} \cdot [\boldsymbol{u}(\boldsymbol{x}+\boldsymbol{\ell}) - \boldsymbol{u}(\boldsymbol{x})]$. K41 asserts that $\delta u_\ell \sim \epsilon^{1/3}\ell^{1/3}$ where ϵ is the total dissipation rate and isotropy is assumed. Thus, for an appropriate averaging operator $\langle ... \rangle$, all increment moments are determined as the structure functions $S^{(p)} = \langle \delta u_\ell^p \rangle = C_p \epsilon^{p/3} \ell^{p/3}$, a form that includes the second-order law $S^{(2)} = C_2 \epsilon^{2/3}\ell^{2/3}$ and (formally) the exact third-order law $S^{(3)} = -(4/3)\epsilon\ell$ as special cases. The refined similarity hypothesis (Kolmogorov 1962, hereafter K62) takes into account intermittency, averaging the local dissipation rate ϵ_ℓ over a volume of linear dimension ℓ and introducing this as an additional random variable. Incorporating the suggestion (Oboukhov 1962) that such irregularity of dissipation changes scalings of increments with ℓ, the refined K62 hypothesis becomes $\delta u_\ell = A(*)\epsilon_\ell^{1/3}\ell^{1/3}$. Here $A(*)$ is a random function that depends on local Reynolds number, but not on ϵ_ℓ or ℓ separately, and takes on a unique form at infinite Reynolds number. For moments $S^{(p)} = \langle \delta u_\ell^p \rangle$, the hypothesis implies

$$S^{(p)} = C_p \langle \epsilon_\ell^{p/3} \rangle \ell^{p/3} = C_p \epsilon^{p/3} \ell^{p/3+\mu(p)}, \quad (1)$$

where $\mu(p)$ is a measure of the intermittency. We define the scaling exponent $\zeta(p) = p/3 + \mu(p)$.

3. Outstanding Observational Questions

The solar wind magnetic field spectrum in the inertial range admits a power law over several decades (Coleman 1966; Matthaeus & Goldstein 1982), although discussion persists concerning exact spectral indices and anisotropy (e.g., Tessein et al. 2009). PDFs of magnetic increments exhibit non-Gaussian features that are increasingly prominent at smaller lags within the inertial range (Sorriso-Valvo et al. 1999). As such, it is understood that the scale-dependent kurtosis $\kappa(\ell)$ (SDK; see Section 5) increases with decreasing ℓ in the inertial range, while higher-order exponents exhibit multifractal scaling (Frisch 1995). Overall, this picture is consistent with expectations from MHD (Carbone et al. 1995; Politano et al. 1998), which in turn are consistent with hydrodynamic scaling (Sreenivasan & Antonia 1997).

The situation is less clear when comparing solar wind statistics in the kinetic range with either MHD or plasma studies. A major issue is the evidence that solar wind subproton-scale kurtosis *decreases* in the kinetic range (Koga et al. 2007; Wan et al. 2012; Chhiber et al. 2018). This is partially at odds with kinetic (Leonardis et al. 2013) and MHD simulation (Wan et al. 2012) as well as observations in the terrestrial magnetosheath (Chhiber et al. 2018). A putative decrease may be due to interference by incoherent waves from foreshock activity, or noise of instrumental or numerical origin (Chian & Miranda 2009; Wu et al. 2013), while a constant SDK may signify a physically relevant transition to mono-fractal scaling (Kiyani et al. 2009; Leonardis et al. 2016). If incoherent plasma waves are the culprit then proximity to the terrestrial bow shock may play a role, and there are some suggestions to this effect in contrasting ACE and Cluster observations (Wan et al. 2012). These issues are resolved below in the PSP observations that we present.

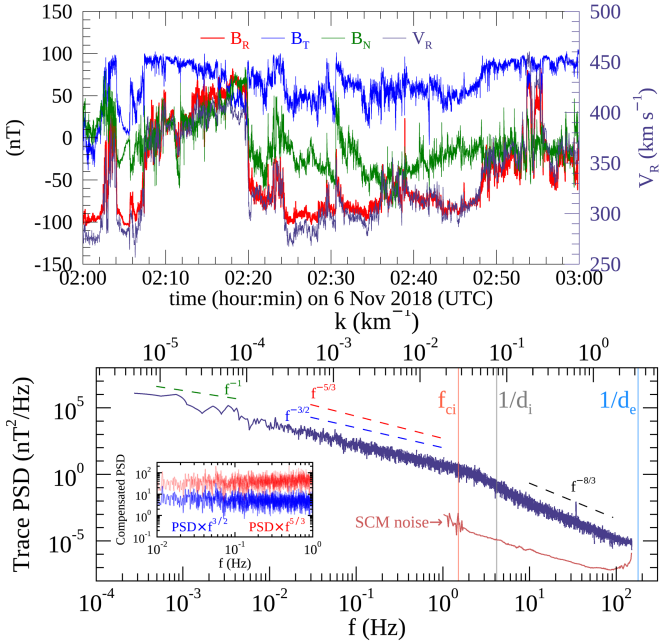

Figure 1. Top: time series of heliocentric *RTN* components of magnetic field, and radial ion velocity. Bottom: trace magnetic field power spectral density (PSD) × 1/3 (dark blue). Instrumental noise floor of SCM (brown). Inset shows compensated PSD. Vertical lines mark ion gyrofrequency f_{ci}, and inverse of ion and electron inertial lengths ($1/d_i$ and $1/d_e$) on wavenumber axis. Equal ion and electron densities are assumed to compute d_e.

4. PSP Observations in Near-Sun Solar Wind

We examine higher-order inertial and kinetic-scale statistics in a region of young solar wind explored for the first time recently by PSP (Fox et al. 2016), using measurements of the magnetic field from the FIELDS instrument (Bale et al. 2016). We focus on a 1 hr interval near first perihelion from UTC 2018 November 6 T02:00:00 to 2018 November 6 T03:00:00, when PSP was at $\sim$35.6 $R_\odot$. We use the SCaM data product, which merges fluxgate and search-coil magnetometer (SCM) measurements by making use of frequency-dependent merging coefficients, thus enabling magnetic field observations from DC to 1 MHz with an optimal signal-to-noise ratio (Bowen et al. 2020). Solar Probe Cup (SPC) data from the SWEAP instrument (Kasper et al. 2016; Case et al. 2020) provide estimates of bulk plasma properties.

For the interval used here, the SCaM data set is resampled to 0.0034 s time cadence. Time series of heliocentric *RTN* components (Fränz & Harper 2002) of the magnetic field are shown in Figure 1. SPC measurements of ion density, velocity, and thermal speed are resampled to 1 s resolution and cleaned using a time-domain Hampel filter (e.g., Pearson 2002). The general properties of the plasma during the interval are listed in Table 1. The radial velocity V_R during this interval indicates a slow wind, with $V_R \lesssim 450\,\mathrm{km\,s^{-1}}$. Three prominent reversals, or switchbacks (Dudok de Wit et al. 2020), of the radial magnetic field are present (see footnote 6). A high degree of correlation, or Alfvénicity, of velocity and magnetic field is observed (Kasper et al. 2019; Chen et al. 2020).

The correlation time (Matthaeus & Goldstein 1982) is $\sim$450 s, corresponding to a correlation length of $\sim 1.5 \times 10^5$ km, using Taylor's frozen-in approximation (Taylor 1938) with a mean speed of 340 $\mathrm{km\,s^{-1}}$. Taylor's hypothesis has reasonable validity during the first PSP orbit (Chhiber et al.

Table 1
Bulk Plasma Parameters

Time on 2018 Nov 6	$\langle V\rangle$	$\langle v\rangle$	$\langle T_{\rm i}\rangle$	$\langle n_{\rm i}\rangle$	$d_{\rm i}$	$\langle B\rangle$	$\langle b\rangle$	$\langle V_{\rm A}\rangle$	$\beta_{\rm i}$
UTC 02:00:00–03:00:00	343 km s^{-1}	52 km s^{-1}	3.8° × 10^5 K	304 cm^{-3}	13 km	99 nT	63 nT	124 km s^{-1}	0.4

Note. Shown are the average values of proton speed $\langle V\rangle \equiv \langle\sqrt{V_R^2+V_T^2+V_N^2}\rangle$, rms velocity fluctuation $\langle v\rangle \equiv \sqrt{\langle|\boldsymbol{V}-\langle\boldsymbol{V}\rangle|^2\rangle}$, ion temperature $\langle T_{\rm i}\rangle$, ion density $\langle n_{\rm i}\rangle$, ion inertial scale $d_{\rm i}$, magnetic field magnitude $\langle B\rangle \equiv \langle\sqrt{B_R^2+B_T^2+B_N^2}\rangle$, rms magnetic fluctuation $\langle b\rangle \equiv \sqrt{\langle|\boldsymbol{B}-\langle\boldsymbol{B}\rangle|^2\rangle}$, Alfvén speed $\langle V_{\rm A}\rangle \equiv \langle B\rangle/\sqrt{4\pi m_{\rm i}\langle n_{\rm i}\rangle}$, and ion beta. Averaging is performed over the entire interval.

2019; Chen et al. 2020); here it is reaffirmed by noting from Table 1 that $\langle v\rangle/\langle V\rangle \sim 0.15$ and $\langle V_{\rm A}\rangle/\langle V\rangle \sim 0.36$.

Figure 1 also shows the average power spectral density of the *RTN* magnetic field components. Similar spectra from PSP have been reported previously (e.g., Chen et al. 2020). We find an inertial range that extends more than two decades in wavenumber; above the ion gyrofrequency the spectrum steepens to a $\sim -8/3$ power law (e.g., Goldstein et al. 2015). Crucial for this work is the signal-to-noise ratio (S/N) at high (kinetic-range) frequencies, where the relevant instrumental noise floor is that of the SCM (Bowen et al. 2020), shown in Figure 1. Clearly S/N $\geqslant 100$ up to 100 Hz, and remains $\geqslant 5$ up to the highest available frequency, providing a measure of confidence that these measurements are unaffected by instrumental noise.

5. Intermittency Observed by PSP

We define increments of magnetic field components at time t as

$$\delta B_i(t,\tau) = B_i(t+\tau) - B_i(t), \tag{2}$$

where $i \in \{R, T, N\}$ and τ is a temporal lag. To convert temporal lags to spatial lags we use the Taylor approximation, wherein the spatial lag corresponding to τ is $\ell = \langle V_R\rangle\tau$ (see Chhiber et al. 2020), with mean radial solar wind speed $\langle V_R\rangle \sim 335$ km s^{-1} here. In this way we obtain spatial increments $\delta B_i(t,\ell)$ using Equation (2). The magnitude of the vector magnetic increment is then $\delta B(t,\ell) \equiv (\delta B_R^2 + \delta B_T^2 + \delta B_N^2)^{1/2}$.

The pth order structure functions of δB are

$$S_B^{(p)}(\ell) = \langle[\delta B(t,\ell)]^p\rangle_T, \tag{3}$$

where the $\langle ...\rangle$ refers to averaging over the time interval $T \gg \tau$. Similarly, for for each component B_i,

$$S_{B_i}^{(p)}(\ell) = \langle[\delta B_i(t,\ell)]^p\rangle_T. \tag{4}$$

The accuracy of computed higher-order moments is affected by sample size; a rule of thumb is that the highest order that can be computed reliably is $p_{\rm max} = \log N - 1$, where N is the number of samples (Dudok de Wit et al. 2013). With $N \sim 1.1\times10^6$ for the present interval we get $p_{\rm max} = 5$. Statistics of higher order than this are interpreted with some reservation.

The top panel of Figure 2 shows $S_B^{(p)}(\ell)$ for p ranging from 1 to 8, and spatial lags ℓ ranging from $\sim 0.1\,d_{\rm i}$, deep within the kinetic range, to $10^4\,d_{\rm i}$, close to the energy-containing scales (the correlation length is $\sim 1.1\times10^4\,d_{\rm i}$). The slopes of $S^{(p)}$ versus ℓ are larger at kinetic scales, indicating the presence of relatively stronger gradients. Structure functions for individual components (Equation (4)) are very similar (not shown).

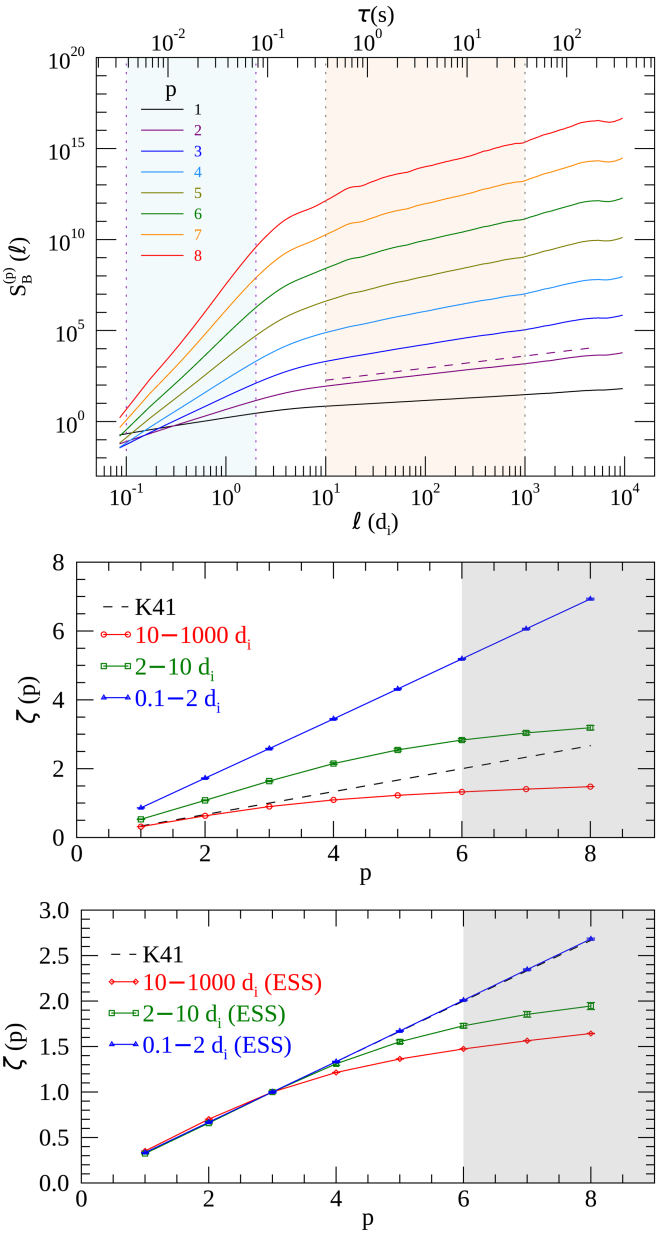

Figure 2. Top: structure functions for δB (Equation (3)) vs. temporal (τ) and spatial (ℓ) lags. A reference $\ell^{2/3}$ curve (dashed, purple) is shown. Shaded region (cream) $\ell = 10 - 10^3\,d_{\rm i}$ demarcates inertial range. Shaded region (blue) $\ell = 0.1{-}2\,d_{\rm i}$ demarcates kinetic range. Middle: scaling exponents $\zeta(p)$ versus p for inertial, kinetic, and intermediate ranges. Dashed line: K41 prediction $\zeta(p) = p/3$. Moments not determined with reliable accuracy: gray-shaded region. 1σ uncertainty estimates for straight line fits to determine $\zeta(p)$ are shown, but are generally smaller than the symbols. Bottom: same as the middle panel, but using ESS; scaling exponents for each range of lags are divided by $\zeta(3)$ for the respective range. Kinetic-range curve (blue triangles) overlaps the K41 curve.

Next we investigate the slopes of the structure functions in greater detail. For Gaussian and nonintermittent statistics consistent with K41 (see Section 2) one expects $S^{(p)}(\ell) \propto \ell^{\zeta(p)}$ with $\zeta(p) = p/3$. Figure 2 (middle panel) shows the scaling exponents $\zeta(p)$ versus p, computed separately for the inertial ($10 - 10^3\, d_i$) and kinetic ($0.1-2\, d_i$) ranges, as well as an intermediate range ($2-10\, d_i$). The exponents are computed by using chi-squared error minimization to fit straight lines to $\ln S^{(p)}$ versus $\ln \ell$. Inertial range exponents (red circles) begin to diverge from the K41 curve beyond $p = 3$, with higher orders showing larger departures, indicating strong intermittency with multifractal statistics (see Equation (1)). The kinetic-range curve (blue diamonds) also lies far from the K41 prediction, but is rather close to a straight line, suggesting monofractal and scale-similar but non-Gaussian statistics. These results are consistent with analyses of near-Earth solar wind turbulence based on Cluster measurements (Kiyani et al. 2009; Alberti et al. 2019). Exponents for the intermediate range show a transition from inertial to kinetic-range behavior.

The bottom panel of Figure 2 employs the extended self-similarity (ESS) hypothesis (Benzi et al. 1993b), which posits that scalings of structure functions at each order are related to that of other orders. In particular the scaling of $S^{(p)}(\ell)$ with order $p > 3$ may relate better to the behavior of $S^{(3)}(\ell)$ than to the lag ℓ itself. Accordingly we proceed by dividing $\zeta(p)$ for the different lag ranges by $\zeta(3)$ for the respective range. This rescaling does not affect the inertial range result significantly. Remarkably, the kinetic-scale exponents collapse almost perfectly to the K41 line. As far as we are aware, this has not been previously demonstrated for magnetic fluctuations in the solar wind. Similar use of ESS has been applied in kinetic simulations (Leonardis et al. 2016; Wan et al. 2016) and to solar wind density fluctuations at subproton scales (Chen et al. 2014). The intermediate range once again exhibits transitional behavior.[5]

To further investigate near-Sun kinetic-scale intermittency we examine PDFs of increments of B_R at lags ranging from near energy-containing scales, through the inertial range, down to subproton scales. We first normalize increments (Equation (2)) at each lag by the corresponding standard deviation, and then compute PDFs by calculating the relative frequency of occurrence of increments within designated bins and dividing these frequencies by the bin width to obtain probability densities. The resulting PDFs (Figure 3) are compared with a Gaussian PDF for reference. Increments at $\ell = 5000\, d_i$ measure structures at scales of about half a correlation length, and these nonuniform, "system-size" structures exhibit a highly irregular PDF, which nevertheless has the narrowest tails of all. PDFs for the two inertial range lags (100 and $10\, d_i$) show wide, super-Gaussian tails, signifying the presence of outlying "extreme" events and intermittency. The $10\, d_i$ lag has slightly wider tails, consistent with the well-known property of stronger intermittency at smaller inertial-range scales (e.g., Sorriso-Valvo et al. 1999; Chhiber et al. 2018).

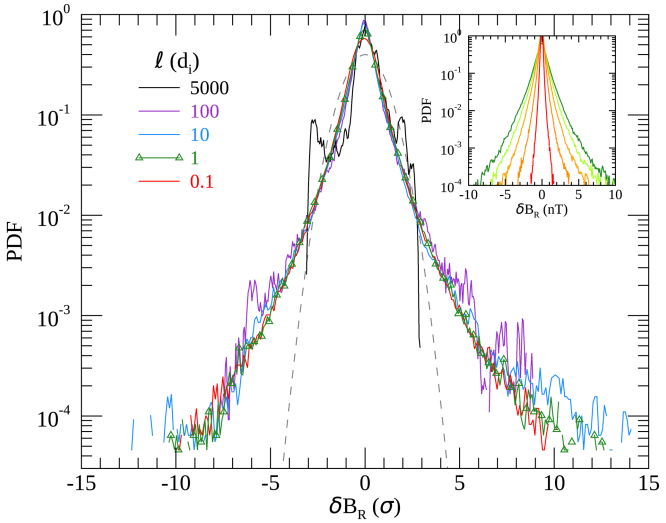

Figure 3. PDFs of δB_R normalized by their standard deviation σ. Gaussian PDF shown for reference (dashed line). Inset: PDFs of unnormalized δB_R; lags from 1 d_i (outermost curve, green) to 0.1 d_i (innermost, red). Collapse of green and red curves after rescaling is evident in the main graphic. All PDFs include bins with population $\geqslant 5$.

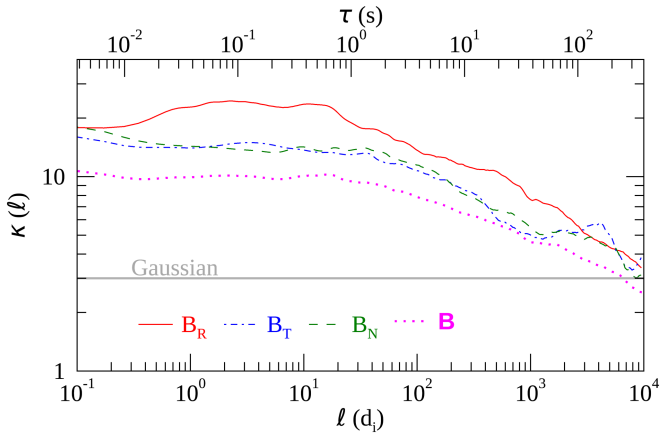

Figure 4. Scale-dependent kurtosis of the magnetic field.

Moving on to kinetic-range lags (1 and 0.1 d_i), we see super-Gaussian tails in PDFs, indicating the continued presence of intermittent structures at these scales. However, the widths of these tails are comparable to (perhaps even slightly narrower than) the $10\, d_i$ case, suggesting a saturation of the level of intermittency at proton scales (see also Figure 4). Furthermore, the scale similarity suggested by the investigation of scaling exponents in the kinetic range (Figure 2) is reaffirmed by the fact that PDFs of the 1 and 0.1 d_i lags overlap to large degree. To emphasize this "monoscaling," the inset in Figure 3 shows PDFs of increments of B_R for $\ell = \{0.1, 0.3, 0.5, 0.8, 1\}\, d_i$, *not* normalized by the respective standard deviations as in the main graphic. The outermost (green) curve is for $\ell = 1\, d_i$ and the innermost (red) curve is for $\ell = 0.1\, d_i$. The scale-similar monoscaling of the PDFs is demonstrated by the fact that these PDFs collapse onto each other after being rescaled by their standard deviations (see Kiyani et al. 2009; Osman et al. 2015). PDFs of δB_T and δB_N behave similarly.

The final diagnostic of intermittency we examine is the SDK, a normalized fourth-order moment that emphasizes the tails of

[5] The present application of ESS is somewhat at variance with the original usage (Benzi et al. 1993b), where the significance of $\zeta(3)$ derives from its correspondence to the third-order energy transfer law. This connection is lost in a plasma because the energy flux involves *mixed* third-order structure functions of both magnetic and velocity fields (Politano & Pouquet 1998); in this sense ESS should properly be based on mixed correlators (Politano et al. 1998). However, including velocity statistics here is not an option since PSP plasma data are not available at sufficiently high cadence to probe the kinetic range (Case et al. 2020). Nevertheless, the use of ESS as we have implemented it clearly organizes the data in a revealing way.

PDFs presented previously:

$$\kappa(\ell) = \frac{S^{(4)}(\ell)}{[S^{(2)}(\ell)]^2}, \tag{5}$$

where $S^{(p)}$ can be defined using either Equations (3) or (4). $\kappa(\ell)$ may be thought of as the inverse of the filling fraction for structures at scale ℓ, i.e., if $\kappa(\ell)$ increases with decreasing ℓ then the fraction of volume occupied by structures at scale ℓ decreases with decreasing ℓ. The scalar Gaussian distribution has $\kappa = 3$; a value $\kappa > 3$ is a manifestation of wider tails relative to the Gaussian (e.g., DeCarlo 1997).

Figure 4 shows $\kappa(\ell)$ for individual components, as well as the magnitude of $\delta\boldsymbol{B}$. All four cases behave similarly—the kurtosis is near Gaussian at the largest lags, increases to values between 10 and 25 as the lag is decreased across the inertial range to $\sim 10\, d_i$, and then stays roughly constant down to $0.1\, d_i$. Once again, this indicates a saturation of the intermittency and scale-similar, monofractal behavior at kinetic scales.[6] This result is consistent with kinetic simulations and Cluster observations in the solar wind presented by Wu et al. (2013). A likely candidate for producing monofractal kinetic-scale kurtosis is a scale-independent fragmentation of current structures between ion and electron scales, as suggested by some kinetic simulations (Karimabadi et al. 2013). Note the marked contrast to Figure 8 of Chhiber et al. (2018), where SDK is re-Gaussianized at kinetic scales presumably due to terrestrial foreshock activity and/or instrumental noise in MMS measurements.

6. Discussion and Conclusions

In this Letter we investigated intermittency in near-Sun solar wind observations of inertial and kinetic-range magnetic turbulence, using standard measures including SDK and scaling of higher-order moments up to eighth. Use of a unique PSP FIELDS data set, merged from fluxgate magnetometer and SCM measurements (Bowen et al. 2020), enables study of high frequencies well into the subproton scales, taking Taylor's hypothesis into account. Our main results extended several prior studies and clarified outstanding questions concerning solar wind intermittency. First, we observed clearly a monofractal, non-Gaussian, subproton kinetic range, consistent with near-Earth observations (Alberti et al. 2019; Kiyani et al. 2009). In particular, with PSP data close to the Sun at 36 $R_\odot$, far from any foreshock activity, and measurements unaffected by noise (Koga et al. 2007; Chian & Miranda 2009; Wan et al. 2012; Wu et al. 2013; Chhiber et al. 2018), it is possible to establish clearly that the kurtosis does not re-Gaussianize at sub-ion scales and the statistics remain intermittent. Another major result of interest from the perspective of turbulence theory (Benzi et al. 1993b, 1993a) is that implementation of ESS for sub-ion scales causes a collapse to linear, Kolmogorov-like behavior for the scaling exponents—consistent with results reported for kinetic simulation (Wan et al. 2016). As far as we are aware this has not been previously demonstrated for magnetic fluctuations in the solar wind. Finally, we report evidence that the magnetic field in near-Sun solar wind exhibits multifractal scaling in the inertial range (see Zhao et al. 2020; Alberti et al. 2020), which is consistent with near-Earth observations (Bruno 2019, and references therein), as well as kinetic simulations of turbulence (Leonardis et al. 2016; Wan et al. 2016). Multifractal inertial-range scaling of higher-order moments is a familiar result in large turbulent MHD systems (Politano et al. 1998; Wan et al. 2012).

We emphasize that the present results are enabled by the unique orbital position of PSP, along with the high-cadence low-noise character of the FIELDS/SCaM magnetic field data set. Even with the clarifications this analysis provides, there remain unanswered questions. One major outstanding issue is why the subproton range becomes monofractal. This implies self-similarity (or "rescaling") of the underlying PDF over that range (e.g., Kiyani et al. 2009). One possible interpretation is that the range between proton and electron scales is populated by scale-invariant sheet-like concentrations of electric current density. In fact, large numbers of highly dynamic subproton-scale current sheets are seen in kinetic simulations (e.g., Karimabadi et al. 2013) and have been inferred in observations (e.g., Retinò et al. 2007). This may be distinguished from an effect of incoherent linear (noninteracting) waves, which may be expected to produce a return to Gaussianity (Koga et al. 2007; Chhiber et al. 2018), and not an onset of monofractal scaling. However, a rigorous connection of structure with monofractality remains to be established and is deferred to future research.

We thank A. Chasapis for useful discussions. This research was supported in part by the PSP mission under the IS⊙IS project (contract NNN06AA01C) and a subcontract to University of Delaware from Princeton (SUB0000165), and NASA HSR grant 80NSSC18K1648. We acknowledge the PSP mission for use of the data, which are publicly available at the NASA Space Physics Data Facility (https://spdf.gsfc.nasa.gov/). FIELDS data are publicly available at https://fields.ssl.berkeley.edu/data/.

Appendix
Relating the intermittency Parameter to the Scaling of Kurtosis

Here we briefly examine the relationship between the intermittency parameter $\mu(p)$ and the scaling behavior of SDK. From Equations (1) and (5) we get

$$\kappa(\ell) = C_\kappa \times \ell^{\mu(4)-2\mu(2)} = C_\kappa \ell^{-\alpha}, \tag{A1}$$

where C_κ is a constant and we have defined

$$\alpha = 2\mu(2) - \mu(4). \tag{A2}$$

For homogeneous K41 turbulence we have $\mu(p) = 0$ for all p, and $\kappa(\ell)$ is constant. For K62 turbulence the intermittency parameters $\mu(*)$ may be nonzero, and, within a range of lags defined by either monofractality or multifractality, C_κ does not vary with cascade rate or ℓ but may depend (in hydrodynamics) on the local Reynolds number (Kolmogorov 1962). For monofractal behavior $\zeta(p) = p/3 + \mu(p)$ is linear in p, and therefore $\mu(4) = 2\mu(2)$, which implies a scale-invariant κ, i.e., κ is constant function of ℓ. Indeed, from the middle panel of Figure 2 we find for the monofractal kinetic range (blue curve) that $\mu(2) = 1.73$ and $\mu(4) = 3.45$, so that $\mu(4) = 1.99\mu(2)$.

[6] To test the robustness of our results and their sensitivity to interval selection (stationarity), the analysis was repeated separately for the first and second halves of the interval, as well as the "quiet" period between 02:20 and 02:50 (see Figure 1). The results were essentially unchanged, although SDK in the quiet period is relatively smaller and flattens at relatively larger scales (tens of d_i), suggesting weaker multifractality in the inertial range.

Finally, for multifractal statistics one expects $|\mu(4)| > |\mu(2)|$, but if κ is a decreasing function of ℓ (as is generally observed) then α remains positive, and the observed exponent α constrains $\mu(2)$ and $\mu(4)$. From Figure 4 we have $\alpha \approx 0.17$ for the pink curve in the inertial range ($\ell = 20-10^3\, d_i$); from the middle panel of Figure 2, we find for the inertial range (red curve) that $2\mu(2) - \mu(4) = 0.17$. Therefore, the relationship between the scaling behavior of the SDK and the intermittency parameter is well described by Equations (A1) and (A2).

ORCID iDs

Rohit Chhiber https://orcid.org/0000-0002-7174-6948
William H. Matthaeus https://orcid.org/0000-0001-7224-6024
Trevor A. Bowen https://orcid.org/0000-0002-4625-3332
Stuart D. Bale https://orcid.org/0000-0002-1989-3596

References

Abramenko, V., Yurchyshyn, V., & Wang, H. 2008, ApJ, 681, 1669
Alberti, T., Consolini, G., Carbone, V., et al. 2019, Entrp, 21, 320
Alberti, T., Laurenza, M., Consolini, G., et al. 2020, ApJ, 902, 84
Bale, S. D., Goetz, K., Harvey, P. R., et al. 2016, SSRv, 204, 49
Benzi, R., Ciliberto, S., Baudet, C., Ruiz Chavarria, G., & Tripiccione, R. 1993a, EL, 24, 275
Benzi, R., Ciliberto, S., Tripiccione, R., et al. 1993b, PhRvE, 48, R29
Borovsky, J. E. 2008, JGRA, 113, A08110
Bowen, T. A., Bale, S. D., Bonnell, J. W., et al. 2020, JGRA, 125, e27813
Bruno, R. 2019, E&SS, 6, 656
Burlaga, L. F. 1991, JGR, 96, 5847
Carbone, V., Veltri, P., & Bruno, R. 1995, PhRvL, 75, 3110
Case, A. W., Kasper, J. C., Stevens, M. L., et al. 2020, ApJS, 246, 43
Chen, C. H. K. 2016, JPlPh, 82, 535820602
Chen, C. H. K., Bale, S. D., Bonnell, J. W., et al. 2020, ApJS, 246, 53
Chen, C. H. K., Sorriso-Valvo, L., Šafránková, J., & Němeček, Z. 2014, ApJL, 789, L8
Chhiber, R., Chasapis, A., Bandyopadhyay, R., et al. 2018, JGRA, 123, 9941
Chhiber, R., Goldstein, M. L., Maruca, B. A., et al. 2020, ApJS, 246, 31
Chhiber, R., Usmanov, A. V., Matthaeus, W. H., Parashar, T. N., & Goldstein, M. L. 2019, ApJS, 242, 12
Chian, A. C.-L., & Miranda, R. A. 2009, AnGeo, 27, 1789
Coleman, P. J. 1966, PhRvL, 17, 207
DeCarlo, L. T. 1997, Psychol. Methods, 2, 292
Dudok de Wit, T., Alexandrova, O., Furno, I., Sorriso-Valvo, L., & Zimbardo, G. 2013, SSRv, 178, 665
Dudok de Wit, T., Krasnoselskikh, V. V., Bale, S. D., et al. 2020, ApJS, 246, 39
Fox, N. J., Velli, M. C., Bale, S. D., et al. 2016, SSRv, 204, 7
Fränz, M., & Harper, D. 2002, P&SS, 50, 217
Frisch, U. 1995, Turbulence. The Legacy of A. N. Kolmogorov (Cambridge: Cambridge Univ. Press)
Goldstein, M. L., Wicks, R. T., Perri, S., & Sahraoui, F. 2015, RSPTA, 373, 20140147
Karimabadi, H., Roytershteyn, V., Wan, M., et al. 2013, PhPl, 20, 012303
Kasper, J. C., Abiad, R., Austin, G., et al. 2016, SSRv, 204, 131
Kasper, J. C., Bale, S. D., Belcher, J. W., et al. 2019, Natur, 576, 228
Kiyani, K. H., Chapman, S. C., Khotyaintsev, Y. V., Dunlop, M. W., & Sahraoui, F. 2009, PhRvL, 103, 075006
Koga, D., Chian, A. C.-L., Miranda, R. A., & Rempel, E. L. 2007, PhRvE, 75, 046401
Kolmogorov, A. 1941, DoSSR, 30, 301
Kolmogorov, A. N. 1962, JFM, 13, 82
Leonardis, E., Chapman, S. C., Daughton, W., Roytershteyn, V., & Karimabadi, H. 2013, PhRvL, 110, 205002
Leonardis, E., Sorriso-Valvo, L., Valentini, F., et al. 2016, PhPl, 23, 022307
Matthaeus, W. H., & Goldstein, M. L. 1982, JGR, 87, 6011
Matthaeus, W. H., Wan, M., Servidio, S., et al. 2015, RSPTA, 373, 20140154
Matthaeus, W. H., Yang, Y., Wan, M., et al. 2020, ApJ, 891, 101
Monin, A. S., & Yaglom, A. M. 1971, Statistical Fluid Mechanics: Mechanics Of Turbulence (Cambridge, MA: MIT Press)
Oboukhov, A. M. 1962, JFM, 13, 77
Osman, K. T., Kiyani, K. H., Matthaeus, W. H., et al. 2015, ApJL, 815, L24
Osman, K. T., Matthaeus, W. H., Wan, M., & Rappazzo, A. F. 2012, PhRvL, 108, 261102
Pearson, R. K. 2002, IEEE Tran. Control Syst. Technol., 10, 55
Politano, H., & Pouquet, A. 1998, PhRvE, 57, R21
Politano, H., Pouquet, A., & Carbone, V. 1998, EL, 43, 516
Retinò, A., Sundkvist, D., Vaivads, A., et al. 2007, NatPh, 3, 236
Roberts, O. W., Verscharen, D., Narita, Y., et al. 2020, PhRvR, 2, 043253
Sorriso-Valvo, L., Carbone, V., Veltri, P., Consolini, G., & Bruno, R. 1999, GeoRL, 26, 1801
Sreenivasan, K. R., & Antonia, R. A. 1997, AnRFM, 29, 435
Taylor, G. I. 1938, RSPSA, 164, 476
Tessein, J. A., Matthaeus, W. H., Wan, M., et al. 2013, ApJL, 776, L8
Tessein, J. A., Smith, C. W., MacBride, B. T., et al. 2009, ApJ, 692, 684
Wan, M., Matthaeus, W. H., Roytershteyn, V., et al. 2016, PhPl, 23, 042307
Wan, M., Osman, K. T., Matthaeus, W. H., & Oughton, S. 2012, ApJ, 744, 171
Wan, M., Oughton, S., Servidio, S., & Matthaeus, W. H. 2009, PhPl, 16, 080703
Wu, P., Perri, S., Osman, K., et al. 2013, ApJL, 763, L30
Zhao, L. L., Zank, G. P., Adhikari, L., et al. 2020, ApJ, 898, 113